magnetochemistry

MDPI

Article

Enhancement of Spin Wave Transmission Through Antiferromagnet in Pt/NiO/CoFeB Heterostructure

Wei Shi [1], Yangkai Wang [2], Zhixin Liu [2], Yilin Pei [1], Qiuping Huang [1,3,4], Zhengping Fu [1,2,3,4], Jianlin Wang [1,3,*] and Yalin Lu [1,2,3,4,*]

[1] Hefei National Research Center for Physical Sciences at the Microscale, University of Science and Technology of China, Hefei 230026, China
[2] Department of Materials Science and Engineering, University of Science and Technology of China, Hefei 230026, China
[3] Anhui Laboratory of Advanced Photon Science and Technology, University of Science and Technology of China, Hefei 230026, China
[4] Hefei National Laboratory, University of Science and Technology of China, Hefei 230088, China
* Correspondence: wangjl@ustc.edu.cn (J.W.); yllu@ustc.edu.cn (Y.L.)

Abstract: A significant enhancement of the spin current transmission through the antiferromagnetic insulating material NiO in Pt/NiO/CoFeB heterostructures was observed in this work. The ultrafast spin currents excited by laser pulses were injected into the Pt layers after passing through the NiO layers, and then transient charge currents were generated via the inverse spin Hall effect (ISHE), leading to a terahertz (THz) emission from the structure. The emitted THz signals were measured using electro-optic sampling with a ZnTe crystal. Thin NiO layers remarkably enhanced the THz signal amplitude, suggesting high spin transfer efficiency in NiO, and lighting a direction to ameliorate the spintronic THz emitter. The variable temperature measurements showed the amplitude had a maximum near the Néel temperature (T_N) of the NiO layer with a specific thickness. The results of phase difference suggested that the coherent evanescent spin wave-mediated transmission had a contribution below the T_N of the NiO layer, while the thermal magnon-mediated transmission existed at all temperatures. Our results not only achieve an enhancement in the spintronic THz source but also provide a THz spectroscopic method to investigate the dynamics of the ultrafast spintronic phenomenon.

Keywords: terahertz; spintronic terahertz emitter; antiferromagnet; spin current; evanescent spin wave

check for updates

Academic Editor: Federico Montoncello

Received: 12 December 2024
Revised: 12 January 2025
Accepted: 20 January 2025
Published: 22 January 2025

Citation: Shi, W.; Wang, Y.; Liu, Z.; Pei, Y.; Huang, Q.; Fu, Z.; Wang, J.; Lu, Y. Enhancement of Spin Wave Transmission Through Antiferromagnet in Pt/NiO/CoFeB Heterostructure. *Magnetochemistry* **2025**, *11*, 7. https://doi.org/10.3390/magnetochemistry11020007

Copyright: © 2025 by the authors. Licensee MDPI, Basel, Switzerland. This article is an open access article distributed under the terms and conditions of the Creative Commons Attribution (CC BY) license (https://creativecommons.org/licenses/by/4.0/).

1. Introduction

The terahertz (THz) window is generally defined as the frequency range 0.3–30 THz in the electromagnetic spectrum. As this region coincides with many fundamental resonances of materials [1–3], THz technology shows promising applications in materials analysis [4,5], biomedicine [6,7], communication [8], imaging [9], and spectroscopy [10]. The utilization of THz technology necessitates the development of high-performance THz sources. Recently, spintronic terahertz emitters (STEs) based on the spin-to-charge conversion have considerably impacted THz technology [11–13], becoming a viable and alternative source to traditional nonlinear crystals [14,15] and photoconductive antennas [16–18], due to the advantages of low cost, ultrathin film, broadband, and optional pumping wavelength. Since the appearance of STEs, numerous strategies have been proposed to enhance the THz signal [13,19–23]. However, there still remains a significant demand for achieving higher intensity, which is crucial for meeting the practical requirements of applications [24,25].

The structures of STEs typically consist of nanometer ferromagnetic (FM)/nonmagnetic (NM) metal junctions [11,12]. Magnetized in-plane and excited by an incident femtosecond laser pulse, the FM layer would inject a spin current pulse j_s into the NM layer [11,12,21]. In the NM layer, the inverse spin Hall effect (ISHE) converts the spin current pulse j_s into an ultrafast transverse charge current j_c [26], thereby acting as a source of THz radiation, following [21]

$$j_c = \gamma j_s \times M/|M| \quad (1)$$

$$< j_c(\omega) >= - < \sigma(\omega) > E(\omega) \quad (2)$$

where γ is the spin Hall angle, M is the sample magnetization, $<\sigma(\omega)>$ is the averaged THz conductivity, and $E(\omega)$ is the emitted THz transient. Traditional improvement strategies generally focus on different material compositions and geometrical stacking of FM/NM layers with a variety of thicknesses [13,19–21], interface engineering of the FM/NM interface [22], and special patterns [23].

The rise of antiferromagnetic (AFM) spintronics has led to various studies on spin current transmission in antiferromagnets [27–30]. The transfer of spin current was usually studied in a FM/AFM/NM trilayer structure [31]. The spin pumping process, spin Seebeck effect, or spin Hall effect can be used to generate and inject a spin current into the AFM layer, in which the driving forces are microwave, temperature gradient, and charge current, respectively [26,32,33]. The spin current transmitted through the AFM layer was detected by a voltage in the adjacent heavy metal via ISHE. The antiferromagnetic order can mediate the spin current efficiently. Especially, several groups have reported that for a certain optimum thickness of the AFM layer, the detected spin current had a maximum that could be even higher than in the absence of the AFM spacer [27–30]. However, most of the investigations were conducted at frequencies much lower than the THz range and measured using the dc method. If this phenomenon could be verified at a THz frequency, it would provide an innovative route to improve the STEs. Moreover, by analyzing the emitted THz signals, we can collect the time domain information of the spin current transmission through AFMs, helping us further understand the physical mechanism.

In this work, we developed a high-intensity STE with a FM/AFM/NM trilayer structure. We deposited a series of Pt/NiO/$Co_{40}Fe_{40}B$ nanofilm heterostructures while varying the thicknesses of the typical antiferromagnet of NiO interlayers. The THz emission spectra revealed an enhancement in the THz signal amplitude with NiO thicknesses below 3 nm, peaking at 2 nm. Additionally, in the variable temperature experiments, the amplitude exhibited a peak near the Néel temperature (T_N) of the NiO layer with a specific thickness. The observed phase difference indicated that the evanescent spin wave-mediated transmission had a contribution below the T_N of the NiO layer.

2. Materials and Methods

2.1. Sample Fabrication

Figure 1a shows a schematic illustration of the device structure. The Pt(6)/NiO(t_{NiO})/$Co_{40}Fe_{40}B$(3) heterostructures with NiO thicknesses t_{NiO} = 1, 2, 3, 4, 6, 8, and 10 nm and capped with a SiO_2(20) layer (numbers represent thicknesses in nm) were grown on 500 μm thick (111)-oriented MgO substrates by magnetron sputtering. The base pressure of the sputtering chamber was below 1×10^{-6} mTorr. The SiO_2 capping layer serves as protection for the underlying layers from oxidation. The rate of film growth was determined by X-ray reflection (XRR) as shown in the Supplementary Materials, Figure S1a. The Ni L edge X-ray absorption spectra (XAS) of the NiO film are shown in the Supplementary Materials, Figure S1b. The X-ray diffraction (XRD) $\theta-2\theta$ patterns of a Pt(6)/NiO(20) bilayer film deposited on MgO (111) substrate (see Figure 1b) indicate that the NiO films are polycrystalline with a

preferred orientation along <111>. A cross-sectional high-resolution transmission electron microscopy (TEM) image of a Pt(6)/NiO(2)/CoFeB(3) multilayer sample is presented in Figure 1c, verifying the thickness of each layer. Figure 1d illustrates cross-sectional energy dispersive X-ray spectroscopy (EDS) Co, Ni, and Pt mapping under the high-angle annular dark field scanning transmission electron microscopy (HAADF-STEM) mode, revealing clear interfaces without diffusion. Therefore, the Pt(6)/NiO(t_{NiO})/CoFeB(3) heterostructures maintain a high interface quality in our experiment. The interfacial effect of different samples on the spin current transmission could be considered the same.

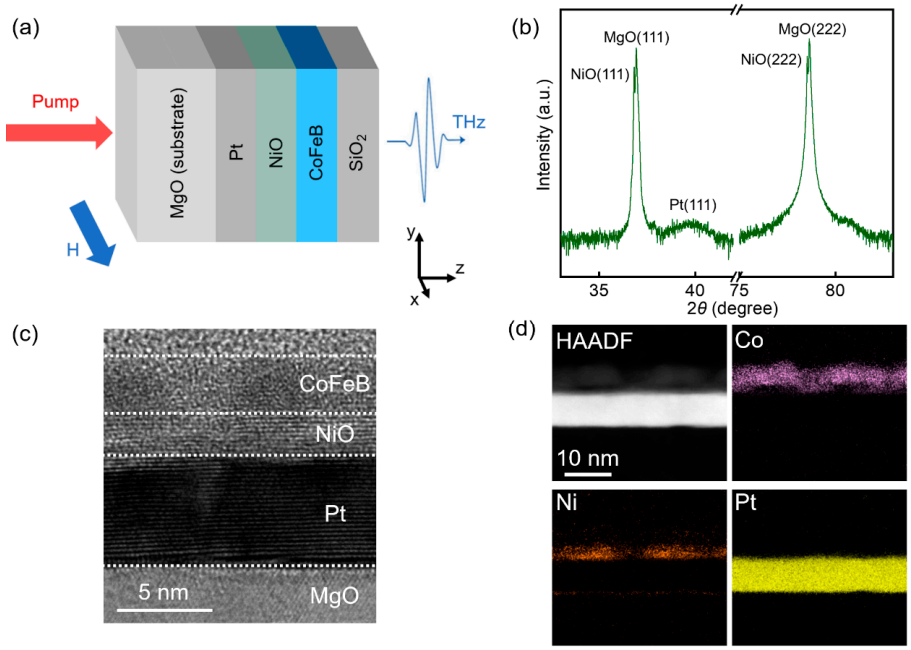


Figure 1. (**a**) Schematic illustration of THz emission with a femtosecond laser pump incident from the substrate side along the *z*-direction and an external magnetic field *H* along the *x*-direction. (**b**) The XRD pattern of a Pt(6)/NiO(20) bilayer film. (**c**) Cross-sectional high-resolution transmission electron microscopy image of a Pt(6)/NiO(2)/CoFeB(3) multilayer sample. (**d**) Cross-sectional high-angle annular dark field scanning transmission electron microscopy (HAADF-STEM) image and energy-dispersive X-ray spectroscopy (EDS) mapping of Co, Ni, and Pt.

2.2. THz Emission Spectroscopy Measurement

Figure 2 illustrates the terahertz emission spectroscopy system. In our experiment, we used a 1 kHz repetition rate Ti: Sapphire laser system with a pulse duration of 35 fs at an 800 nm central wavelength (Spitfire-Ace, Spectra Physics). The laser beam was split into two parts at a ratio of 8:2: the large one was focused on the sample with a spot size of approximately 3 mm in diameter and an average pump fluence of 720 μJ·cm^{-2} to excite the ferromagnetic layer-generating spin current to emit terahertz waves, and the small one was used to detect the THz pulse. The excitation laser was incident on the sample along the *z*-axis. (see Figure 1a). An external magnetic field (*H*) of 700 Oe was applied to keep the CoFeB in saturated magnetization along the *y*-axis. The THz emission with the electric field along the *x*-axis was collected by a pair of parabolic mirrors and then measured using electro-optic sampling with a 500 μm thick (110)-oriented ZnTe crystal. In general, the laser can be incident from both sides. However, in this work, the laser was incident from the substrate side to avoid undesired THz absorption by the substrate (see emitted THz signal of both sides in the Supplementary Materials, Figure S2a). The THz emission experiment was conducted in a dry air atmosphere to prevent water vapor absorption.

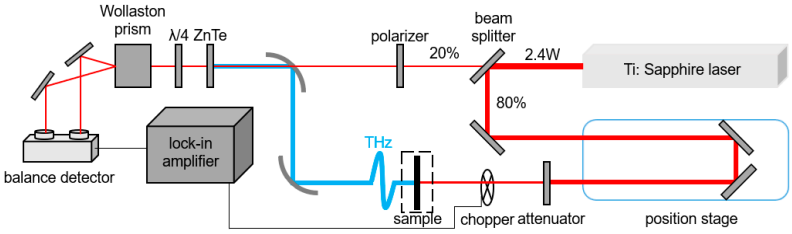


Figure 2. Schematic diagram of terahertz emission spectroscopy system.

3. Results and Discussion

3.1. The THz Emission with Different NiO Thicknesses

Figure 3a illustrates the emitted THz signals of the Pt(6)/NiO(t_{NiO})/CoFeB(3) multilayer films with different NiO thicknesses, t_{NiO} = 0, 1, 2, 3, 4, 6, 8, and 10 nm [t_{NiO} = 0 for Pt(6)/CoFeB(3)], under the same experimental conditions. The shape of the THz pulses stayed constant with different NiO thicknesses. The dependence between the peak amplitude of the THz signal and the thickness of the NiO interlayer is shown in Figure 3b. The peak amplitude of the THz signal increased and then decreased exponentially after reaching a maximum at t_{NiO} = 2 nm. For t_{NiO} = 1, 2, and 3 nm, the emitted THz signals were much larger than even that in the original Pt(6)/CoFeB(3) sample. Figure 3c demonstrates the frequency domain THz spectra of Pt(6)/CoFeB(3) and Pt(6)/NiO(2)/CoFeB(3); the enhancement exists in a wide frequency range. At the maximum point (t_{NiO} = 2 nm), the amplitude reached approximately 110% of commercial ZnTe crystals under the same pump power (see the comparison in Supplementary Materials, Figure S3). This unique enhancement effect is consistent with former dc measurements on the spin transmission of thin NiO layers [27–29].

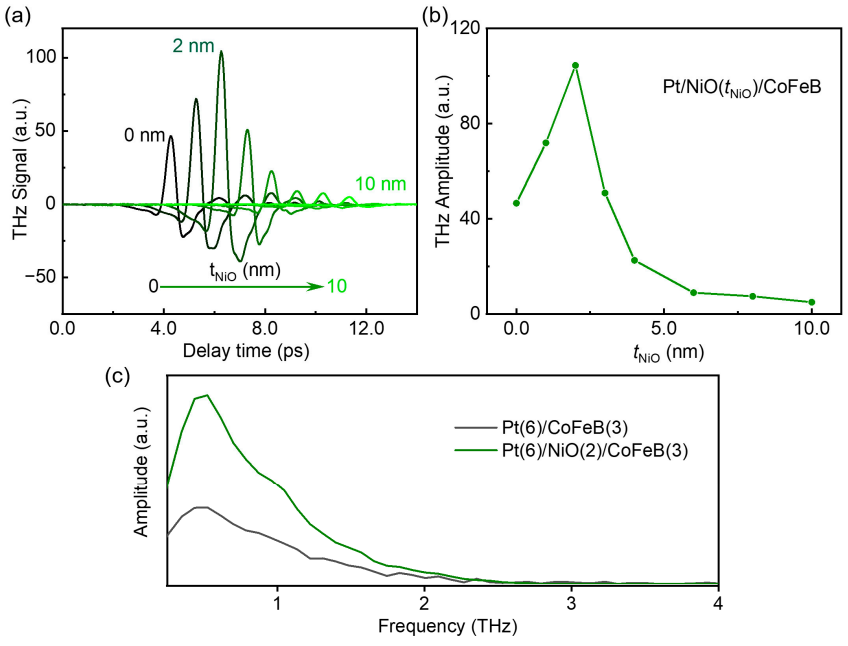


Figure 3. (**a**) Emitted THz signals of the Pt(6)/NiO(t_{NiO})/CoFeB(3) multilayer samples with different NiO thicknesses. The data are shifted horizontally for clarity. (**b**) The dependence between the peak amplitude of the THz signal and the thickness of NiO interlayer. (**c**) The frequency domain THz spectra of Pt(6)/CoFeB(3) and Pt(6)/NiO(2)/CoFeB(3).

3.2. The THz Emission with Different Pump Fluences and Rotations

In order to investigate the enhancement effect in the NiO layer, a series of experiments were performed on two samples: Pt(6)/CoFeB(3) as the reference sample and

Pt(6)/NiO(2)/CoFeB(3) as the interlayer sample. The THz signal amplitudes emitted from these samples were analyzed under varying pump fluences, as depicted in Figure 4a. Both the reference and interlayer samples exhibited similar trends in THz signal amplitudes in response to increasing pump fluences. Specifically, the signal displayed a predominantly linear growth at low fluences and nonlinear growth at higher fluences. Notably, both samples reached a saturation point at approximately 1800 μJ·cm^{-2}, below the thermal damage fluence threshold (~5000 μJ·cm^{-2}) [34–36], suggesting that the presence of the NiO interlayer did not influence the infrared absorption efficiency of the sample. Furthermore, the ratio of the emitted THz signals remained consistent across the entire fluence range, demonstrating that the transmission of spin current remained stable and unaffected by variations in pump fluence.

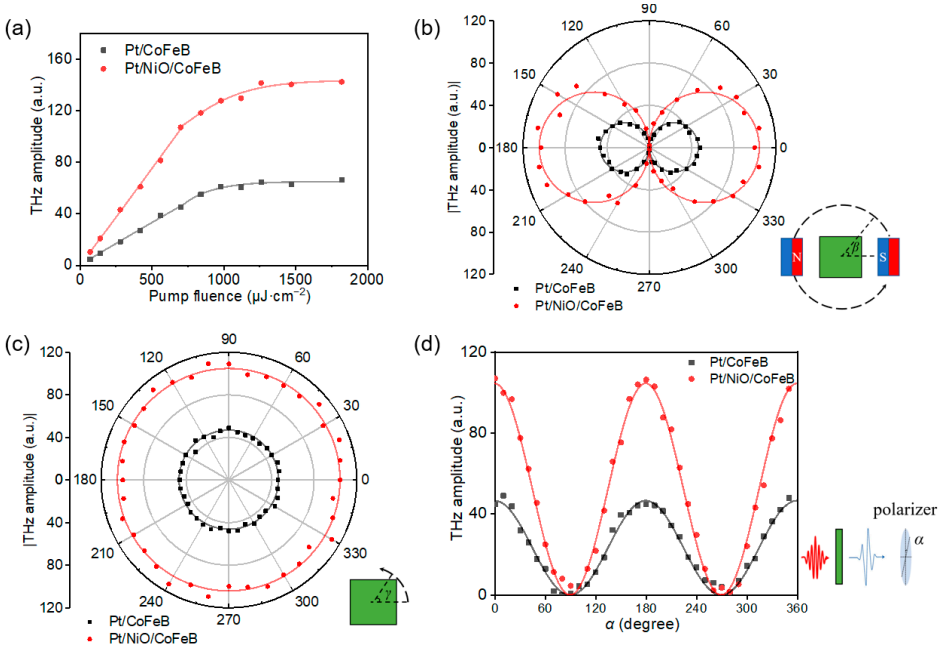


Figure 4. (**a**) The pump fluence dependence of the THz signal amplitude emitted from Pt(6)/CoFeB(3) (black squares) and Pt(6)/NiO(2)/CoFeB(3) (red circles). The solid lines represent fitting eye-guiding lines. (**b**) THz amplitude as a function of the magnetic field rotation angle β. The solid lines are curve-fit proportional to $|\cos\beta|$. (**c**) THz amplitude as a function of the sample rotation angle γ. The solid lines are constant fits. (**d**) Relationship between THz amplitude and polarizer rotation angle α. The solid lines are curve-fit proportional to $\cos^2\alpha$.

Fixing the position and angle of the interlayer sample and the reference sample, we adjusted the direction of the magnetic field. The signal amplitude in relation to the magnetic field angle (β) is illustrated in Figure 4b. The experimental data are well fitted by the function $E_{\mathrm{THz}} \propto \cos\beta$, which is consistent with Equation (1). The phase of the THz signal undergoes a 180° shift when the direction of the magnetic field is reversed (see emitted THz signals under different magnetic field directions in the Supplementary Materials, Figure S2b). With the magnetic field fixed along the x-axis, the azimuth of the samples was rotated. Figure 4c demonstrates that the THz amplitude remains relatively constant irrespective of the rotation angle (γ), indicating isotropic behavior and suggesting that anisotropy in the (111)-oriented NiO interlayer does not affect spin current transmission. The variation in THz amplitude due to adjustments in the angle (α) of the polarizer positioned behind the sample is depicted in Figure 4d. The experimental data are well fitted by the function $E_{\mathrm{THz}} \propto E_0\cos^2\alpha$. Here, E_0 represents the THz amplitude at $\alpha = 0$. These THz emission characteristics reveal that ISHE still plays a key role in the spin-to-charge conversion

without coupling other mechanisms in the interlayer sample. As a result, we can analyze the spin current j_s with the emitted THz signal E_{THz}, according to Equations (1) and (2).

3.3. The Temperature Dependence of the THz Emission

Variable-temperature THz emission measurements were conducted in a cryostat with optical windows and cooled by liquid nitrogen. In Figure 5a, the temperature dependences of the emitted THz amplitude in Pt(6)/NiO(t_{NiO})/CoFeB(3) for t_{NiO} = 0, 1, 2, 3, and 4 nm are presented. Due to the quartz windows (with ~50% transmittance in the THz range), the signals are weaker compared to those in Figure 4. In the absence of the NiO interlayer, the THz amplitude of Pt(6)/CoFeB(3) remains relatively constant for T between 80 K and 300 K. However, with the NiO layer inserted, the THz amplitude of Pt/NiO/CoFeB exhibits distinct temperature dependence, showing a well-defined broad peak. For t_{NiO} = 1, 2, 3, and 4 nm, the peak temperature progressively increases. According to Equations (1) and (2), with the same Pt layer and the same experimental conditions, the spin current j_s passing through the NiO layer has a linear relationship with the emitted THz signal E_{THz},$j_s \propto E_{THz}$. Therefore, the transmission efficiency of the NiO layer can be defined as the ratio $j_s(t_{NiO})/j_s(0) = E_{THz}(t_{NiO})/ E_{THz}(0)$ (see Figure 5b). The results in Figure 5b of $E_{THz}(t_{NiO})/ E_{THz}(0)$ appear similar to those in Figure 5a because $E_{THz}(0)$ for Pt/CoFeB without the NiO interlayer varies minimally. As shown in Figure 5b, the presence of the intervening NiO layer significantly enhances the spin current, up to a factor of 4.0 for the 2 nm thick NiO.

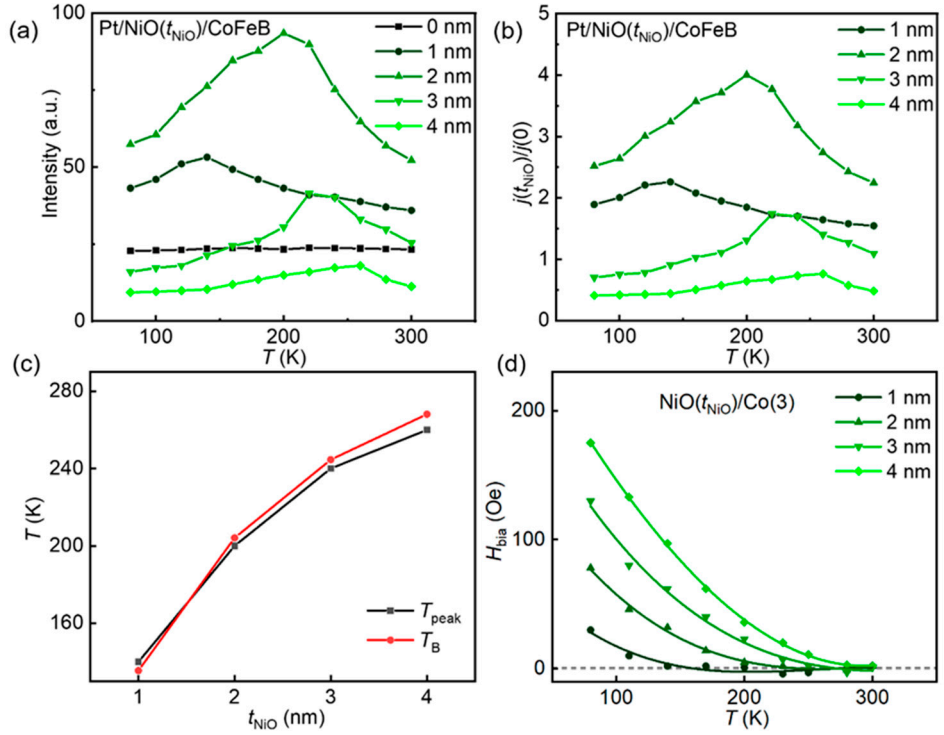


Figure 5. The temperature dependences of (**a**) the THz amplitude and (**b**) the transmission efficiency $j_s(t_{NiO})/j_s(0)$ in Pt(6)/NiO(t_{NiO})/CoFeB(3) for t_{NiO} = 0, 1, 2, 3, and 4 nm. (**c**) The peak temperature T_{peak} (black squares) and the blocking temperature T_B (red circles) as a function of t_{NiO}. (**d**) Temperature dependences of exchange bias field H_{bia} in NiO(t_{NiO})/Co(3) films. The curves are fitting lines, and the dashed line is H_{bia} = 0.

The enhancement of j_s has a well-defined peak at T_{peak}, with values of 140 K, 200 K, 240 K, and 260 K strongly depending on t_{NiO} = 1, 2, 3, and 4 nm. As shown in Figure 5c, T_{peak} increases logarithmically with the thickness of the NiO layer. A similar characteristic is

also observed in $Y_3Fe_5O_{12}$/CoO/Pt by spin pumping [28]. The T_{peak} is close to the reduced Néel temperature $T_N(t_{NiO})$ of the isolated thin NiO layer due to finite size effects [28,37,38]. The value of $T_N(t_{NiO})$ can be estimated by the blocking temperature T_B at which the exchange bias of a ferromagnetic layer exchange coupled to the NiO vanishes [39]. The blocking temperature is close to and usually slightly lower than T_N [37]. As shown in the Supplementary Materials, Figure S4, the magnetic hysteresis loop of a NiO(1)/Co(3) bilayer film shifts to a positive field at T = 80 K after cooling down from 300 K at a 1 T field, due to the exchange bias [39,40]. From the temperature dependence of the exchange bias field shown in Figure 5d, the blocking temperature T_B of the NiO layer with t_{NiO} = 1, 2, 3, and 4 nm could be calculated. As shown in Figure 5c, for every NiO layer thickness, T_{peak} is close to T_B. This suggests a connection between the spin current transmission and the AFM order.

3.4. The Phase Spectra of the THz Emission

The spin current transmission mechanism in AFM insulators is generally discussed in terms of coherent evanescent spin waves [41] with other theoretical models [42–44]. Both the evanescent wave-mediated model and the thermal magnon-mediated model could explain the thickness dependence and temperature dependence of the enhancement effect. One of the most significant differences between them is the phase shift caused by the AFM layer, following [41]

$$P \propto \cos(\varphi - \pi/2) \tag{3}$$

where P is the spin current passing through the AFM layer, φ is the phase shift between the input spin current and output spin current. Therefore, if the spin current was efficiently mediated by the evanescent spin waves, a phase shift $\varphi \approx \pi/2$ would be measured [45]. However, typical studies on spin current transmission across AFMs are always restricted to dc detection [27–30], which cannot capture the phase information.

To address the question of whether the spin current is carried by coherent evanescent spin waves within the AFM [41], the emitted THz signals from Pt/CoFeB (as input) and Pt/NiO/CoFeB (as output) are Fourier transformed to obtain the phase spectra. Figure 6a demonstrates the phase spectra of Pt(6)/CoFeB(3) and Pt(6)/NiO(2)/CoFeB(3) at 80 K, where the bandwidth is limited by the detection crystal. The phase of the Pt(6)/NiO(2)/CoFeB(3) THz emission signal distinctly deviates from that of Pt(6)/CoFeB(3) (see the phase spectra of Pt(6)/MgO(2)/CoFeB(3) and Pt(6)/Cu(2)/CoFeB(3) in the Supplementary Materials, Figure S5). Particularly, around 1.0 THz, which is one of the frequencies of the evanescent AFM spin wave modes of NiO [41], the phase difference is about 90°. This reveals the existence of the evanescent spin wave-mediated transmission.

Figure 6b shows the temperature dependences of the phase shifts in Pt(6)/NiO(t_{NiO})/CoFeB(3) for t_{NiO} = 1, 2, 3, and 4 nm. The plotted phase shifts have average values near 1.0 THz (±0.1 THz). The 90° phase shift is quite stable when the temperature is below the blocking temperature T_B in Figure 5c. Beyond T_B, with rising temperature, the phase shift decreases sharply to about 0°. This suggests that the evanescent spin wave-mediated transmission can only happen below the Néel temperature T_N of the AFM layer, as the theoretical model predicted [41]. Moreover, the evanescent spin wave-mediated transmission exhibits frequency selectivity, and the phase shift is closer to 90° near the frequencies of the evanescent AFM spin wave modes. This might explain the absence of a coherent evanescent spin wave mode in Py/Ag/CoO/Ag/$Fe_{75}Co_{25}$/MgO(001) in Ref. [46], which was based on GHz spin currents. On the other hand, at a temperature beyond T_N, the THz emission signal still exists with little phase shift. This should be the result of the thermal magnon-mediated transmission [43] (see Figure 6c).

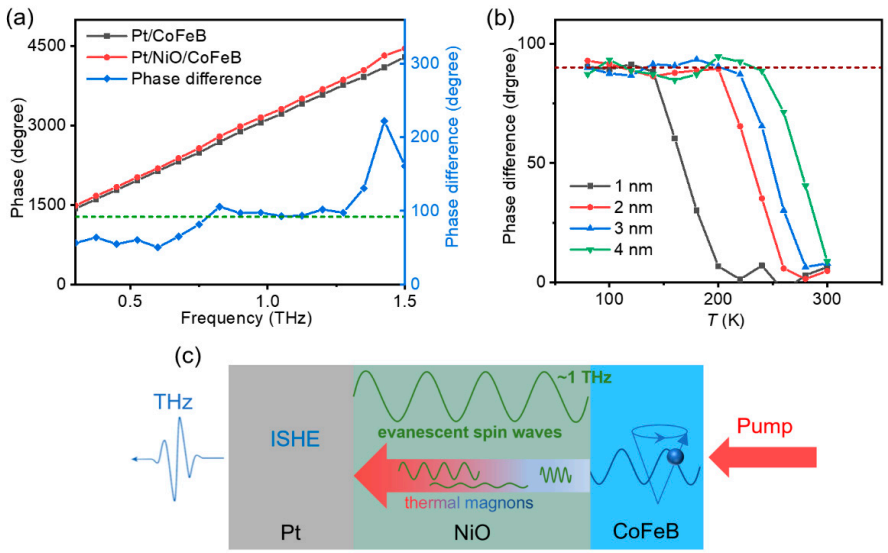


Figure 6. (**a**) The phase spectra of Pt(6)/CoFeB(3) (black squares) and Pt(6)/NiO(2)/CoFeB(3) (red circles) at 80 K. The blue diamonds are the phase difference between them. The green dashed line is in the position of 90° ($\pi/2$). (**b**) The temperature dependences of the phase differences in Pt(6)/NiO(t_{NiO})/CoFeB(3) for t_{NiO} = 1, 2, 3, and 4 nm. The plotted phase differences have average values near 1.0 THz. (**c**) Schematic diagram of the spin current transmission through antiferromagnetic insulating material NiO in Pt/NiO/CoFeB heterostructures.

4. Conclusions

In summary, we have systematically studied the THz emission from the Pt/NiO/CoFeB heterostructure. The spin current was enhanced for NiO thicknesses less than 3 nm, in a manner consistent with previously reported experimental measurements of dc spin current and theoretical studies, resulting in a remarkable enhancement in the THz emission. The THz emission amplitude reached a maximum near the T_N of the NiO layer of a specific thickness. The phase difference results show that the coherent evanescent spin wave-mediated transmission has a contribution below the T_N of the NiO layer, and the thermal magnon-mediated transmission exists at all temperatures. These findings open a route for enhancement in the spintronic THz source and deepen our understanding of the spin current transmission across AFM insulators. We believe that this THz spectroscopic method would be effective for other research on the dynamic of the spintronic phenomenon involving spin currents.

Supplementary Materials: The following supporting information can be downloaded at: https://www.mdpi.com/article/10.3390/magnetochemistry11020007/s1, Figure S1: X-ray reflection (XRR) and Ni L edge X-ray absorption spectra(XAS) of thin films; Figure S2: THz signals of different magnetic field directions and both sides; Figure S3: Comparison between the THz signals emitted from a Pt(6)/NiO(2)/CoFeB(3) multilayer film and commercial ZnTe crystal; Figure S4: The exchange bias field Hbia in NiO(t_{NiO})/Co(3) films; Figure S5: The phase spectra of Pt(6)/MgO(2)/CoFeB(3) and Pt(6)/Cu(2)/CoFeB(3).

Author Contributions: Conceptualization, data curation, methodology, and writing—original draft, W.S.; software, W.S. and Y.W.; investigation, W.S., Y.W., Z.L., Y.P. and Q.H.; formal analysis, W.S., Y.W., Z.L., Y.P. and Q.H.; project administration, Q.H., Z.F., J.W. and Y.L.; supervision, Z.F., J.W. and Y.L.; writing—review and editing, J.W. and Y.L.; funding acquisition, J.W. and Y.L. All authors have read and agreed to the published version of the manuscript.

Funding: This research was funded by the National Key Research and Development Program of China of the Ministry of Science and Technology (2023YFA1610100); the National Science Foundation

of China (51627901); the Key Research and Development Program of Anhui Province (2022a05020051); and the Natural Science Foundation of Anhui Province (2208085ME113).

Data Availability Statement: The data used to support the findings of this study are available from the corresponding author upon request.

Conflicts of Interest: The authors declare no conflicts of interest.

References

1. Ferguson, B.; Zhang, X.-C. Materials for terahertz science and technology. *Nat. Mater.* **2002**, *1*, 26–33. [CrossRef] [PubMed]
2. Ho, L.; Pepper, M.; Taday, P. Terahertz spectroscopy: Signatures and fingerprints. *Nat. Photonics* **2008**, *2*, 541–543. [CrossRef]
3. Shi, X.; Han, Z. Enhanced terahertz fingerprint detection with ultrahigh sensitivity using the cavity defect modes. *Sci. Rep.* **2017**, *7*, 13147. [CrossRef] [PubMed]
4. Dikmelik, Y.; Spicer, J.B.; Fitch, M.J.; Osiander, R. Effects of surface roughness on reflection spectra obtained by terahertz time-domain spectroscopy. *Opt. Lett.* **2006**, *31*, 3653. [CrossRef]
5. Nguyen, D.T.; Pissard, A.; Pierna, J.A.F.; Rogez, H.; Souza, J.; Dortu, F.; Goel, S.; Hernandez, Y.; Baeten, V. A method for non-destructive determination of cocoa bean fermentation levels based on terahertz hyperspectral imaging. *Int. J. Food Microbiol.* **2022**, *365*, 109537. [CrossRef]
6. Yang, X.; Zhao, X.; Yang, K.; Liu, Y.; Liu, Y.; Fu, W.; Luo, Y. Biomedical applications of terahertz spectroscopy and imaging. *Trends Biotechnol.* **2016**, *34*, 810–824. [CrossRef]
7. El-Shenawee, M.; Vohra, N.; Bowman, T.; Bailey, K. Cancer detection in excised breast tumors using terahertz imaging and spectroscopy. *Biomed. Spectrosc. Imaging* **2019**, *8*, 1–9. [CrossRef]
8. Liu, K.; Feng, Y.; Han, C.; Chang, B.; Chen, Z.; Xu, Z.; Li, L.; Zhang, B.; Wang, Y.; Xu, Q. High-speed 0.22 THz communication system with 84 Gbps for real-time uncompressed 8K video transmission of live events. *Nat. Commun.* **2024**, *15*, 8037. [CrossRef]
9. Luo, Y.; Jelic, V.; Chen, G.; Nguyen, P.H.; Liu, Y.-J.R.; Calzada, J.A.M.; Mildenberger, D.J.; Hegmann, F.A. Nanoscale terahertz STM imaging of a metal surface. *Phys. Rev. B* **2020**, *102*, 205417. [CrossRef]
10. Tonouchi, M. Cutting-edge terahertz technology. *Nat. Photonics* **2007**, *1*, 97–105. [CrossRef]
11. Seifert, T.S.; Cheng, L.; Wei, Z.; Kampfrath, T.; Qi, J. Spintronic sources of ultrashort terahertz electromagnetic pulses. *Appl. Phys. Lett.* **2022**, *120*, 180401. [CrossRef]
12. Seifert, T.; Jaiswal, S.; Martens, U.; Hannegan, J.; Braun, L.; Maldonado, P.; Freimuth, F.; Kronenberg, A.; Henrizi, J.; Radu, I.; et al. Efficient metallic spintronic emitters of ultrabroadband terahertz radiation. *Nat. Photonics* **2016**, *10*, 483–488. [CrossRef]
13. Wu, Y.; Elyasi, M.; Qiu, X.; Chen, M.; Liu, Y.; Ke, L.; Yang, H. High-performance THz emitters based on ferromagnetic/nonmagnetic heterostructures. *Adv. Mater.* **2017**, *29*, 1603031. [CrossRef]
14. Zhang, X.-C.; Ma, X.F.; Jin, Y.; Lu, T.-M.; Boden, E.P.; Phelps, P.D.; Stewart, K.R.; Yakymyshyn, C.P. Terahertz optical rectification from a nonlinear organic crystal. *Appl. Phys. Lett.* **1992**, *61*, 3080–3082. [CrossRef]
15. Hirori, H.; Doi, A.; Blanchard, F.; Tanaka, K. Single-cycle terahertz pulses with amplitudes exceeding 1 MV/cm generated by optical rectification in $LiNbO_3$. *Appl. Phys. Lett.* **2011**, *98*, 091106. [CrossRef]
16. Auston, D.H.; Shank, C.V. Picosecond ellipsometry of transient electron-hole plasmas in germanium. *Phys. Rev. Lett.* **1974**, *32*, 1120–1123. [CrossRef]
17. Auston, D.H.; Cheung, K.P.; Smith, P.R. Picosecond photoconducting hertzian dipoles. *Appl. Phys. Lett.* **1984**, *45*, 284–286. [CrossRef]
18. Ketchen, M.B.; Grischkowsky, D.; Chen, T.C.; Chi, C.-C.; Duling, I.N.; Halas, N.J.; Halbout, J.-M.; Kash, J.A.; Li, G.P. Generation of subpicosecond electrical pulses on coplanar transmission lines. *Appl. Phys. Lett.* **1986**, *48*, 751–753. [CrossRef]
19. Kumar, N.; Hendrikx, R.W.A.; Adam, A.J.L.; Planken, P.C.M. Thickness dependent terahertz emission from cobalt thin films. *Opt. Express* **2015**, *23*, 14252. [CrossRef]
20. Qiu, H.S.; Kato, K.; Hirota, K.; Sarukura, N.; Yoshimura, M.; Nakajima, M. Layer thickness dependence of the terahertz emission based on spin current in ferromagnetic heterostructures. *Opt. Express* **2018**, *26*, 15247. [CrossRef]
21. Kampfrath, T.; Battiato, M.; Maldonado, P.; Eilers, G.; Nötzold, J.; Mährlein, S.; Zbarsky, V.; Freimuth, F.; Mokrousov, Y.; Blügel, S.; et al. Terahertz spin current pulses controlled by magnetic heterostructures. *Nat. Nanotechnol.* **2013**, *8*, 256–260. [CrossRef] [PubMed]
22. Scheuer, L.; Ruhwedel, M.; Karfaridis, D.; Vasileiadis, I.G.; Sokoluk, D.; Torosyan, G.; Vourlias, G.; Dimitrakopoulos, G.P.; Rahm, M.; Hillebrands, B.; et al. THz emission from Fe/Pt spintronic emitters with $L1_0$-FePt alloyed interface. *iScience* **2022**, *25*, 104319. [CrossRef] [PubMed]
23. Liu, C.; Wang, S.; Zhang, S.; Cai, Q.; Wang, P.; Tian, C.; Zhou, L.; Wu, Y.; Tao, Z. Active spintronic-metasurface terahertz emitters with tunable chirality. *Adv. Photonics* **2021**, *3*, 056002. [CrossRef]

24. Li, X.; Qiu, T.; Zhang, J.; Baldini, E.; Lu, J.; Rappe, A.M.; Nelson, K.A. Terahertz field–induced ferroelectricity in quantum paraelectric $SrTiO_3$. *Science* **2019**, *364*, 1079–1082. [CrossRef]
25. Schlauderer, S.; Lange, C.; Baierl, S.; Ebnet, T.; Schmid, C.P.; Valovcin, D.C.; Zvezdin, A.K.; Kimel, A.V.; Mikhaylovskiy, R.V.; Huber, R. Temporal and spectral fingerprints of ultrafast all-coherent spin switching. *Nature* **2019**, *569*, 383–387. [CrossRef]
26. Saitoh, E.; Ueda, M.; Miyajima, H.; Tatara, G. Conversion of spin current into charge current at room temperature: Inverse spin-Hall effect. *Appl. Phys. Lett.* **2006**, *88*, 182509. [CrossRef]
27. Wang, H.; Du, C.; Hammel, P.C.; Yang, F. Antiferromagnonic spin transport from $Y_3Fe_5O_{12}$ into NiO. *Phys. Rev. Lett.* **2014**, *113*, 097202. [CrossRef]
28. Qiu, Z.; Li, J.; Hou, D.; Arenholz, E.; N'Diaye, A.T.; Tan, A.; Uchida, K.; Sato, K.; Okamoto, S.; Tserkovnyak, Y.; et al. Spin-current probe for phase transition in an insulator. *Nat. Commun.* **2016**, *7*, 12670. [CrossRef]
29. Lin, W.; Chen, K.; Zhang, S.; Chien, C.L. Enhancement of thermally injected spin current through an antiferromagnetic insulator. *Phys. Rev. Lett.* **2016**, *116*, 186601. [CrossRef]
30. Prakash, A.; Brangham, J.; Yang, F.; Heremans, J.P. Spin Seebeck effect through antiferromagnetic NiO. *Phys. Rev. B* **2016**, *94*, 014427. [CrossRef]
31. Hou, D.; Qiu, Z.; Saitoh, E. Spin transport in antiferromagnetic insulators: Progress and challenges. *NPG Asia Mater.* **2019**, *11*, 35. [CrossRef]
32. Uchida, K.; Xiao, J.; Adachi, H.; Ohe, J.; Takahashi, S.; Ieda, J.; Ota, T.; Kajiwara, Y.; Umezawa, H.; Kawai, H.; et al. Spin Seebeck insulator. *Nat. Mater.* **2010**, *9*, 894–897. [CrossRef]
33. Hirsch, J.E. Spin Hall effect. *Phys. Rev. Lett.* **1999**, *83*, 1834–1837. [CrossRef]
34. Paries, F.; Selz, F.; Santos, C.N.; Lampin, J.-F.; Koleják, P.; Lezier, G.; Troadec, D.; Tiercelin, N.; Vanwolleghem, M.; Addda, A.; et al. Optical damage thresholds of single-mode fiber-tip spintronic terahertz emitters. *Opt. Express* **2024**, *32*, 24826. [CrossRef] [PubMed]
35. Vogel, T.; Omar, A.; Mansourzadeh, S.; Wulf, F.; Sabanés, N.M.; Müller, M.; Seifert, T.S.; Weigel, A.; Jakob, G.; Kläui, M.; et al. Average power scaling of THz spintronic emitters efficiently cooled in reflection geometry. *Opt. Express* **2022**, *30*, 20451. [CrossRef] [PubMed]
36. Kumar, S.; Nivedan, A.; Singh, A.; Kumar, Y.; Malhotra, P.; Tondusson, M.; Freysz, E.; Kumar, S. Optical damage limit of efficient spintronic THz emitters. *iScience* **2021**, *24*, 103152. [CrossRef]
37. Ambrose, T.; Chien, C.L. Finite-size effects and uncompensated magnetization in thin antiferromagnetic CoO layers. *Phys. Rev. Lett.* **1996**, *76*, 1743–1746. [CrossRef]
38. Alders, D.; Tjeng, L.H.; Voogt, F.C.; Hibma, T.; Sawatzky, G.A.; Chen, C.T.; Vogel, J.; Sacchi, M.; Iacobucci, S. Temperature and thickness dependence of magnetic moments in NiO epitaxial films. *Phys. Rev. B* **1998**, *57*, 11623–11631. [CrossRef]
39. Ambrose, T.; Chien, C.L. Dependence of exchange coupling on antiferromagnetic layer thickness in NiFe/CoO bilayers. *J. Appl. Phys.* **1998**, *83*, 6822–6824. [CrossRef]
40. Liu, Z.Y.; Adenwalla, S. Closely linear temperature dependence of exchange bias and coercivity in out-of-plane exchange-biased $[Pt/Co]_3$/NiO (11 Å) multilayer. *J. Appl. Phys.* **2003**, *94*, 1105–1109. [CrossRef]
41. Khymyn, R.; Lisenkov, I.; Tiberkevich, V.S.; Slavin, A.N.; Ivanov, B.A. Transformation of spin current by antiferromagnetic insulators. *Phys. Rev. B* **2016**, *93*, 224421. [CrossRef]
42. Takei, S.; Moriyama, T.; Ono, T.; Tserkovnyak, Y. Antiferromagnet-mediated spin transfer between a metal and a ferromagnet. *Phys. Rev. B* **2015**, *92*, 020409. [CrossRef]
43. Bender, S.A.; Skarsvåg, H.; Brataas, A.; Duine, R.A. Enhanced spin conductance of a thin-film insulating antiferromagnet. *Phys. Rev. Lett.* **2017**, *119*, 056804. [CrossRef] [PubMed]
44. Rezende, S.M.; Rodríguez-Suárez, R.L.; Azevedo, A. Diffusive magnonic spin transport in antiferromagnetic insulators. *Phys. Rev. B* **2016**, *93*, 054412. [CrossRef]
45. Dąbrowski, M.; Nakano, T.; Burn, D.M.; Frisk, A.; Newman, D.G.; Klewe, C.; Li, Q.; Yang, M.; Shafer, P.; Arenholz, E.; et al. Coherent transfer of spin angular momentum by evanescent spin waves within antiferromagnetic NiO. *Phys. Rev. Lett.* **2020**, *124*, 217201. [CrossRef]
46. Li, Q.; Yang, M.; Klewe, C.; Shafer, P.; N'Diaye, A.T.; Hou, D.; Wang, T.Y.; Gao, N.; Saitoh, E.; Hwang, C.; et al. Coherent ac spin current transmission across an antiferromagnetic CoO insulator. *Nat. Commun.* **2019**, *10*, 5265. [CrossRef]

Disclaimer/Publisher's Note: The statements, opinions and data contained in all publications are solely those of the individual author(s) and contributor(s) and not of MDPI and/or the editor(s). MDPI and/or the editor(s) disclaim responsibility for any injury to people or property resulting from any ideas, methods, instructions or products referred to in the content.